Supporting information

Excitonic Complexes and Emerging Interlayer Electron-Phonon Coupling in BN Encapsulated Monolayer Semiconductor Alloy: $WS_{0.6}Se_{1.4}$

Yuze Meng[1,2#], Tianmeng Wang[2#], Zhipeng Li[2,3], Ying Qin[4], Zhen Lian[2], Yanwen Chen[2], Michael C. Lucking[6], Kory Beach[6], Takashi Taniguchi[5], Kenji Watanabe[5], Sefaattin Tongay[4], Fengqi Song[1*], Humberto Terrones[6,*], Su-Fei Shi[2,7*]

[1.] College of Physics, Nanjing University, Nanjing, 210093, P. R. China

[2.] Department of Chemical and Biological Engineering, Rensselaer Polytechnic Institute, Troy, NY 12180

[3.] School of Chemistry and Chemical Engineering, Shanghai Jiao Tong University, Shanghai, 200240, China

[4.] School for Engineering of Matter, Transport and Energy, Arizona State University, Tempe, Arizona 85287, USA

[5.] National Institute for Materials Science, 1-1 Namiki, Tsukuba 305-0044, Japan.

[6.] Department of Physics, Applied Physics, and Astronomy, Rensselaer Polytechnic Institute, Troy, NY 12180

[7.] Department of Electrical, Computer & Systems Engineering, Rensselaer Polytechnic Institute, Troy, NY 12180

[#] These authors contributed equally to this work

[*] Corresponding authors: shis2@rpi.edu, terroh@rpi.edu, songfengqi@nju.edu.cn

Section S1. Sample preparation

Monolayer $WS_{0.6}Se_{1.4}$ encapsulated in hexagonal hBN is prepared with propylene carbonate (PPC) thin film by a pick-up method[1]. Monolayer $WS_{0.6}Se_{1.4}$ and few-layer h-BN are prepared by mechanical exfoliation with scotch tape on silicon substrates with a 300 nm oxide layer. We use PPC thin film to pick up top h-BN, monolayer $WS_{0.6}Se_{1.4}$ and bottom hBN in sequence with accurate alignment control under an optical microscope, with a pick-up temperature of 45℃. We further exfoliate uniform few-layer graphene onto Polydimethylsiloxane (PDMS) thin film and transfer it onto the SiO_2/Si substrate with pre-patterned gold electrodes[2] at 40℃. The PPC film with hBN/ $WS_{0.6}Se_{1.4}$/hBN junction is then stamped onto the graphite electrode. We make sure that the monolayer $WS_{0.6}Se_{1.4}$ is not covered completely by the bottom h-BN so it has good contact with the graphite electrode. The stamping temperature is set at 90℃ so that the PPC thin film can be removed easily with the vdW structure left on the SiO_2/Si substrate. The device is then soaked in acetone for 12 hours to remove the PPC residue completely. Finally, another piece of few-layer graphene is transferred onto the top h-BN to work as the top gate electrode.

Section S2. Optical spectroscopy setup for the SHG measurement

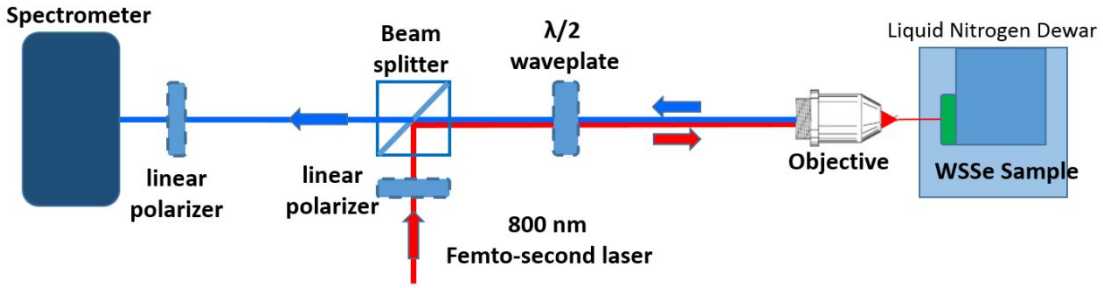

Figure S1. A schematic of the second harmonic generation (SHG) spectroscopy setup.

The optical SHG setup is schematically shown in Fig. S1. We use a pulsed femtosecond laser (Coherent Chameleon Ultra) as the light source for the SHG measurement. The incident laser was chosen to be centered at 800nm, and the laser was focused by a 40X objective (NA: ~0.55) to a spot size of ~ 2 μm. An achromatic half-wave plate (Thorlabs) mounted on a motorized stage was used to change the polarization of the light. Then the SHG signal centered at 400 nm was collected by a CCD camera, after a linear polarizer and spectrograph.

Section S3. The trion splitting from the PL spectra of WS_2

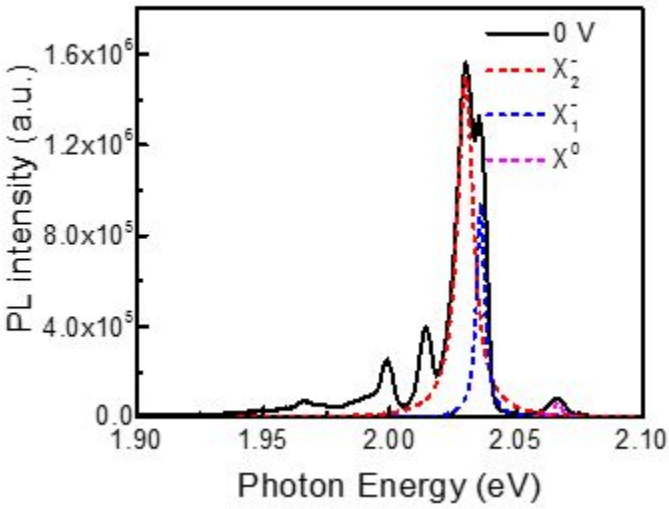

Figure S2. PL spectra of h-BN encapsulated monolayer WS_2 at 14 K. Dashed lines are the Lorentzian fittings for the exciton (magenta), inter-valley trion (blue) and intra-valley trion (red) peaks.

Previous experiments have reported discrepant values for the trion splitting in monolayer WS_2. A few earlier studies reported ~11 meV[3,4], while a recent experimental reported ~ 6 meV in an h-BN sandwiched WS_2 monolayer[5]. To reconcile the discrepancy, we have measured a high-quality h-BN encapsulated WS_2 and determine the splitting to be 6 meV, which is the value we cited in the main text. We measured the PL spectra at 14 K for the monolayer WS_2 encapsulated by h-BN flakes. As shown in Fig. S2, the splitting trion peaks are clearly resolved in the PL spectrum in Fig. S2. The trion binding energy, defined as the energy difference between the exciton and trion,

is 36.7 meV for the intra-valley trion and 30.7 meV for the inter-valley, respectively. The binding energy difference between the two trions is thus 6.0 meV, which is due to the exchange interaction.

Section S4. Gate-dependent PL and reflection spectra of the monolayer $WS_{0.6}Se_{1.4}$

Due to the space limit in the main text, we include here the detailed PL spectra and reflectance spectra of the monolayer $WS_{0.6}Se_{1.4}$ at 14 K, as a function of the gate voltages.

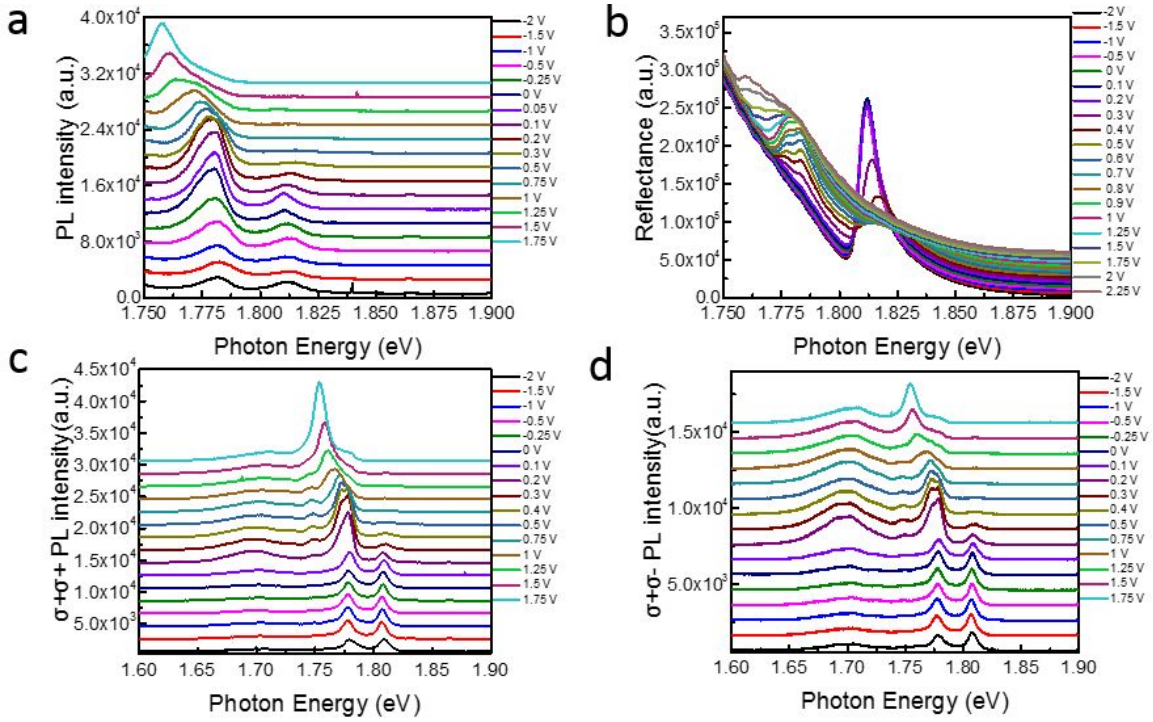

Figure S3. (a) PL spectra of the h-BN encapsulated monolayer $WS_{0.6}Se_{1.4}$ as a function of the gate voltage at the temperature of 14 K. (b) Reflectance spectra of monolayer $WS_{0.6}Se_{1.4}$ as a function of the gate voltage at 14 K. (c) Monolayer $WS_{0.6}Se_{1.4}$ PL spectra with σ+ excitation and σ+ detection at different gate voltages. (d) Monolayer $WS_{0.6}Se_{1.4}$ PL spectra with σ+ excitation and σ- detection at different gate voltages.

Continuous wave (CW) laser centered at 1.960 eV is used as the excitation. Fig. S3a shows the detailed gate dependence of the PL spectra. At the negative gate voltage, neither the exciton nor the trion exhibits significant gate dependence. As the gate voltage increases from 0 to the positive voltage, the exciton peak intensity decreases while the trion peak increase, a result of the increased electron doping in the monolayer $WS_{0.6}Se_{1.4}$. Securitized investigation reveals that the trion peak is not a single Lorentzian peak. Instead, it can be fitted with two peaks which originate from the exchange interaction induced trion splitting. We show the detailed fitting in Section S5.

As the gate voltage exceeds 0.75V, the trion peak disappears, and a new peak emerges. The new peak has been reported previously and was recently assigned to the plasma coupled exciton[6–8].

Fig. S3b shows the reflectance spectra of the device as a function of the gate voltage. The evolution

of the peaks is essentially the same as the PL spectra evolution as shown in Fig. S3a. However, the splitted trions are more clearly resolved.

Fig. S3c,d plot detailed circularly polarized PL spectra of the h-BN encapsulated monolayer $WS_{0.6}Se_{1.4}$ for the $\sigma^+ \sigma^+$ (Fig. 3c) and $\sigma^+ \sigma^-$ (Fig. 3d) configurations. They correspond to the color plots shown in the Fig. 3 of the main text.

Section S5. Fitting of the exciton and trion peaks.

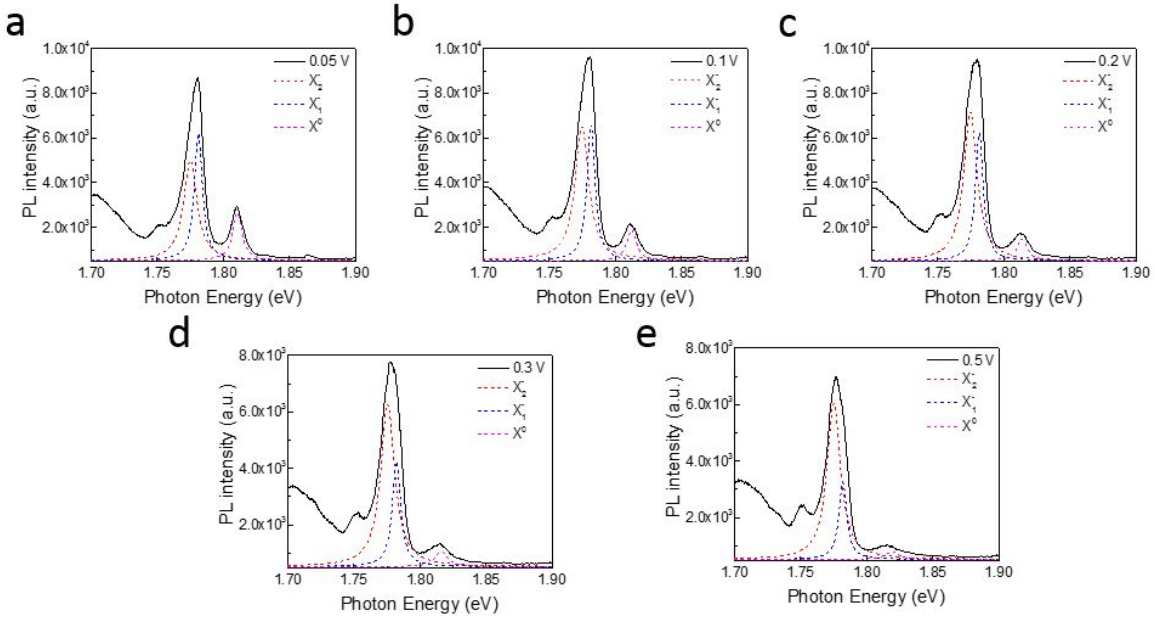

Figure S4. PL spectra of the h-BN encapsulated monolayer $WS_{0.6}Se_{1.4}$ at 14 K when the gate voltage is (a) 0.05 V, (b) 0.1 V, (c) 0.2 V, (d) 0.3 V and (e) 0.5 V. The dashed lines are the Lorentzian fittings of the exciton (magenta), inter-valley trion (blue) and intra-valley trion (red).

The PL of the trion is not a single Lorentzian peak because that it involves the splitting of the two trions. Here we use the two Lorentzian peaks to fit the PL from the trion, and we do so for different gate voltages in the n doping regime to show the evolution as a function of the gate voltage, which is shown in Fig. S4. The ratio of the intra-valley trion and inter-valley trion increases as the gate voltage increases (increased electron doping), leading to the overall red shift of the trion peak.

Section S6. Gate-voltage dependence of the excitonic complexes peak positions

Using the results from section S5, we plot the fittings for the exciton, intra-valley trion and inter-valley trion peak as a function of the gate voltage in Fig. S5a, b, and c, respectively. We also show in Fig. S5d the peak position of the fitting peaks as a function of the gate voltage. The exciton peak exhibits a noticeable blue shift, while neither the intra-valley trion nor the inter-valley trion shows a significant shift. The insensitive gate voltage dependence of the trion peaks determines that the trion splitting is nearly a constant, 6 meV, for different gate voltages. Fig. S5e plots the integrated

intensity as a function of the gate voltage.

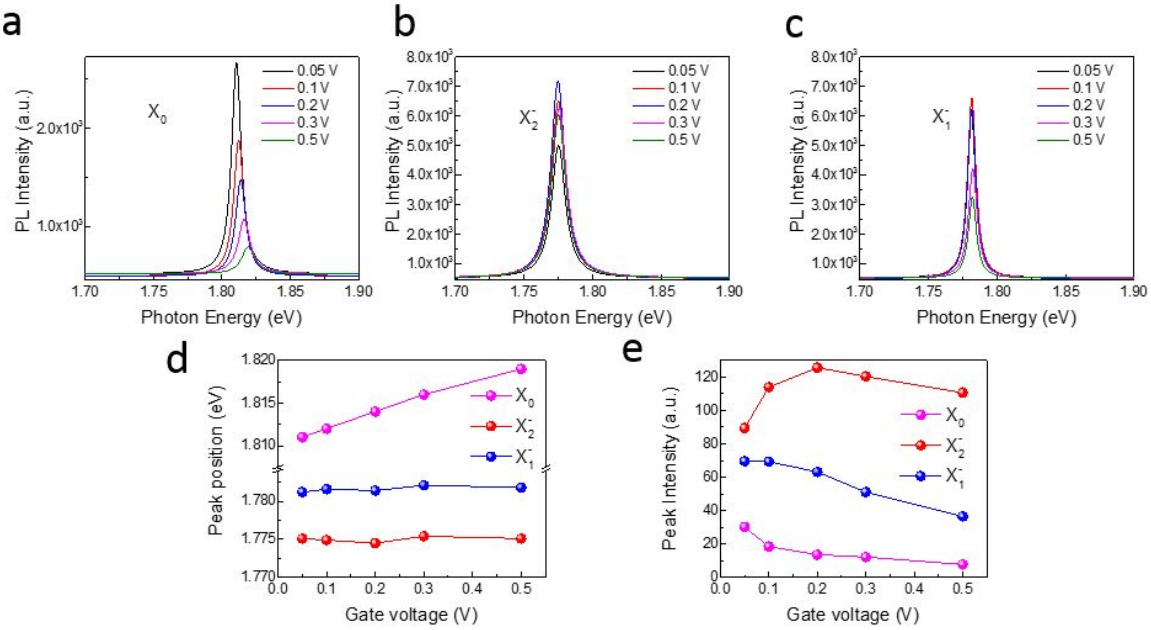

Figure S5. The Lorentzian fittings of the PL from (a) the exciton, (b) the intra-valley trion and (c) the inter-valley trion are plotted as a function of the gate voltages. (d) The peak position of the exciton (magenta), intra-valley trion (red) and inter-valley trion (blue) as a function of the gate voltages. (e) The integrated PL intensity from the fitting for exciton (magenta), intra-valley trion (red) and inter-valley trion (blue) as a function of the gate voltages.

Section S7. Linearly polarized PL spectra of bare monolayer $WS_{0.6}Se_{1.4}$ and BN flakes

To confirm the nature of the emerging peaks (Raman mode I and II in the main text) in the BN encapsulated monolayer $WS_{0.6}Se_{1.4}$ device, we take the control measurements by taking PL spectra of the monolayer $WS_{0.6}Se_{1.4}$ (without BN encapsulation layer) and bare h-BN flake with the linearly polarized excitation and a parallel or cross polarizer at 77 K in Fig. S6. The photoexcitation is a CW laser centered at 1.960 eV. It is evident that the additional Raman peak I and II (shown in the main text) for the BN encapsulated monolayer $WS_{0.6}Se_{1.4}$ are missing in Fig. S6a and S6b. This confirms that the Raman mode I and II are from the interlayer coupling in BN encapsulated monolayer $WS_{0.6}Se_{1.4}$.

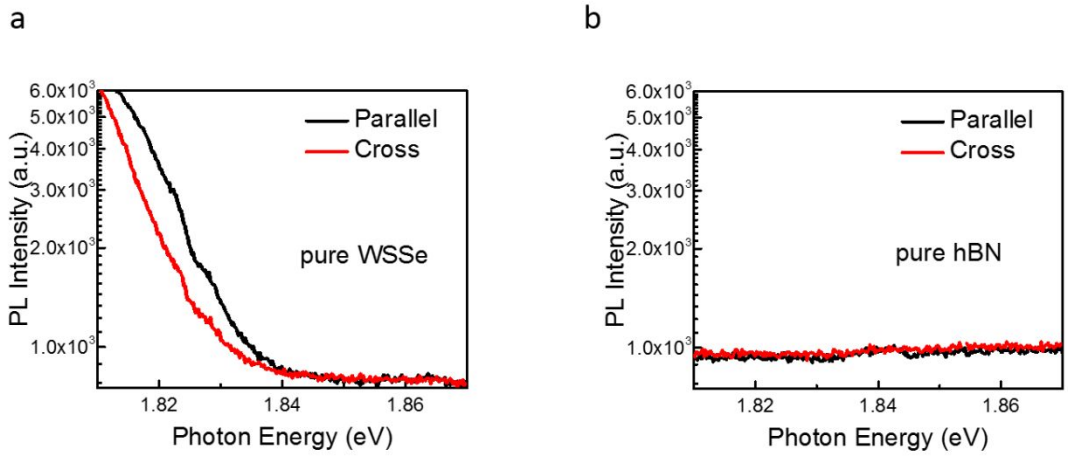

Figure S6 (a) PL spectra of monolayer $WS_{0.6}Se_{1.4}$ (without BN encapsulation) with the linearly polarized excitation, detected by the parallel or cross linear polarizer at 77 K. (b) PL spectra of bare h-BN flake taken with the parallel and cross configuration at 77 K. Spectra in both (a) and (b) are optically excited by a CW laser centered at 1.960 eV

Due to the limited space in the main text, we present part of the wavelength and gate dependence measurements here. Fig. S7a shows PL spectra of another monolayer $WS_{0.6}Se_{1.4}$ device with different photoexcitation at 1.960 eV (red) and 1.951 eV (black) at 14 K, and the spectra were taken with the parallel configuration. The two main emerging peaks I and II showed in the main text, shift position as the photoexcitation energy changes, but the Raman shift stay the same, 813cm^{-1} and 1068cm^{-1}, respectively. As we switch the photoexcitation to 2.331 eV at 77 K, as shown in Fig. S7b, the Raman mode I (813cm^{-1}) is still visible, but the intensity is quenched by more than two orders of magnitude, confirming the resonant nature of the Raman process.

Section S8. Gate-voltage dependence of the emerging mode I and II.

We also show here the detailed gate dependence study of the emerging peak I and II. We took the linearly polarized PL spectra of a monolayer $WS_{0.6}Se_{1.4}$ with photoexcitation at 1.960 eV in the parallel (Fig. S7c) and cross (Fig. S7d) configuration. Because the sensitive dependence on the polarization, we can subtract the PL spectra in the parallel configuration with that in the cross configuration to obtain a background free spectra, with clear emergence of the mode I (~ 1.83 eV) and II (~ 1.86 eV). Both peaks exhibit sensitive dependence on the gate voltage, most pronounced for the gate voltage between -2 V to 0 V and quenched for the positive gate voltage. Based on the behavior of the PL intensity of the A exciton, the monolayer $WS_{0.6}Se_{1.4}$ is close to charge-neutral.

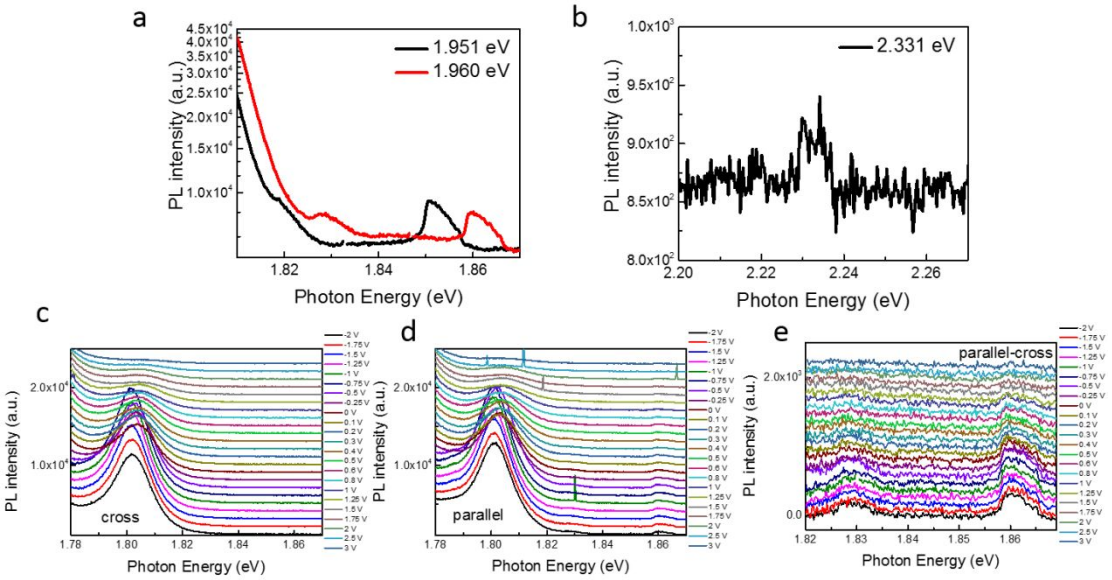

Figure S7 (a) Linearly polarized PL spectra of the BN encapsulated monolayer $WS_{0.6}Se_{1.4}$ device with optical excitation at 1.960 eV (red) and 1.951 eV (black) at the temperature of 14 K. The spectra were taken in the parallel configuration. (b) PL spectra of the monolayer $WS_{0.6}Se_{1.4}$ with photoexcitation at 2.331 eV at 77 K. The spectra were taken at the parallel configuration. (c) PL spectra of the monolayer $WS_{0.6}Se_{1.4}$ as a function of the gate voltage at 77 K. The spectra were taken in the cross configuration with the photoexcitation at 1.960 eV. (d) PL spectra of the monolayer $WS_{0.6}Se_{1.4}$ as a function of the gate voltage at 77 K. The spectra were taken in the parallel configuration with the photoexcitation at 1.960 eV. (e) Linearly polarized PL spectra difference of the monolayer $WS_{0.6}Se_{1.4}$ between the parallel and cross configuration as a function of the gate voltage at 77 K, with the photoexcitation at 1.960 eV. The emerging peak I and II exhibit sensitive dependence on the gate voltage. Note the spectra in (c)-(e) are stacked with an offset for clarification.

Section S9. Gate-voltage dependence of the emerging mode I and II.

To investigate the nature of the new optical resonances (X*), we plot the differential reflectance spectra of the monolayer $WS_{0.6}Se_{1.4}$ as a function of the gate voltage at 14 K in Fig. S8a as a color plot and the detailed spectra for each gate voltage is shown in Fig. S8b. The most pronounced feature around ~1.80 eV is due to the A exciton resonance, whose intensity is most strong at the gate voltage between -2 V to 0 V and start to vanish as the gate voltage exceeds 0 V. A small bump can be observed centered ~ 1.94 eV (indicated by the black arrow in Fig. S8a), which we attribute to the new resonance X*. The intensity of the X* is much weaker than the A exciton resonance, but it can still be seen in the zoom-in of the spectra in Fig. S8b, shown as the gate voltage dependence in Fig. S8c. To illustrate the gate voltage dependence of the X* more clearly, we take the derivative of the spectra in Fig. S8c and show them in Fig. S8d (the color plot is shown in the main text as Fig. 5b). It is evident that the X* exhibit same gate voltage dependence as the A

exciton resonance, which supports our assignment of the new X* resonance to the 2s state of the A exciton.

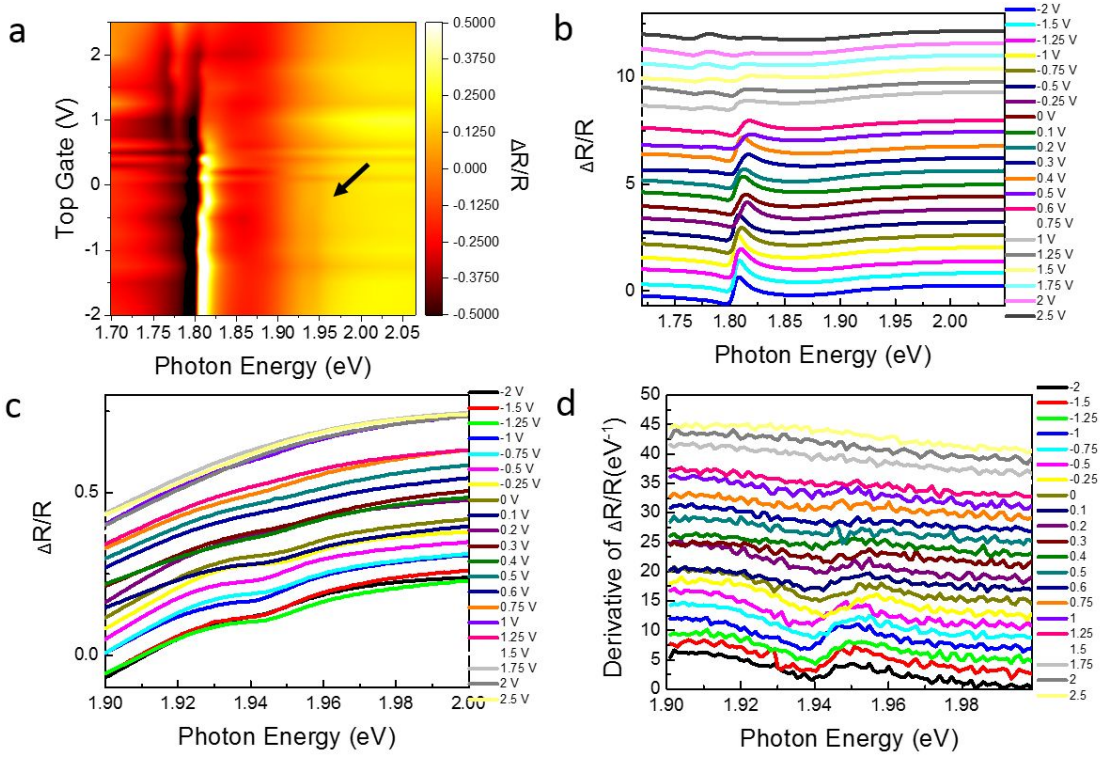

Figure S8 (a) Color plot of the differential reflectance spectra of the monolayer $WS_{0.6}Se_{1.4}$ as a function of the gate voltage at 14 K. The color represents the magnitude of the differential reflectance signal. (b) Differential reflectance spectra of the monolayer $WS_{0.6}Se_{1.4}$ as a function of the gate voltage at 14 K. (c) Zoom-in of the differential reflectance spectra in (b) near 1.94 eV. (d) The derivative of the spectra in (c).

Section S10. Differential reflectance of the device

To confirm that the new optical resonances (X*) is not from the B exciton of $WS_{0.6}Se_{1.4}$, we plot the differential reflectance spectra of the device below in Figure S10. Here we have found the existence of the B exciton of $WS_{0.6}Se_{1.4}$ at 2.22 eV, which is more pronounced than the X* peak. The B exciton lies ~400 meV below the A exciton resonance, similar to the value reported in WSe_2 and WS_2[9].

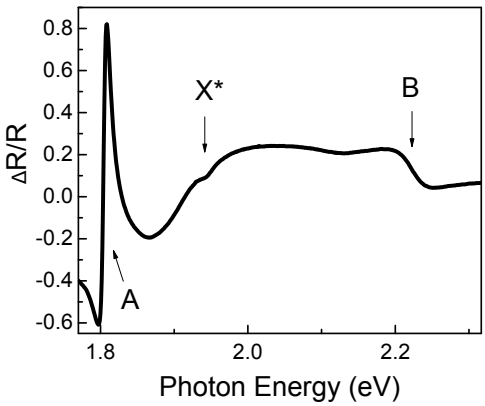

Figure S9. Differential reflectance spectra the BN encapsulated monolayer $WS_{0.6}Se_{1.4}$ at 14 K.

Section S11. AFM measurement

We show below the AFM measurement of the piece of the hBN flake used in our device 2 (data shown in Fig. S10). We note that all the BN flakes we chose as top gate dielectric show similar color contrast under an optical microscope, and they should be similar in terms of thickness.

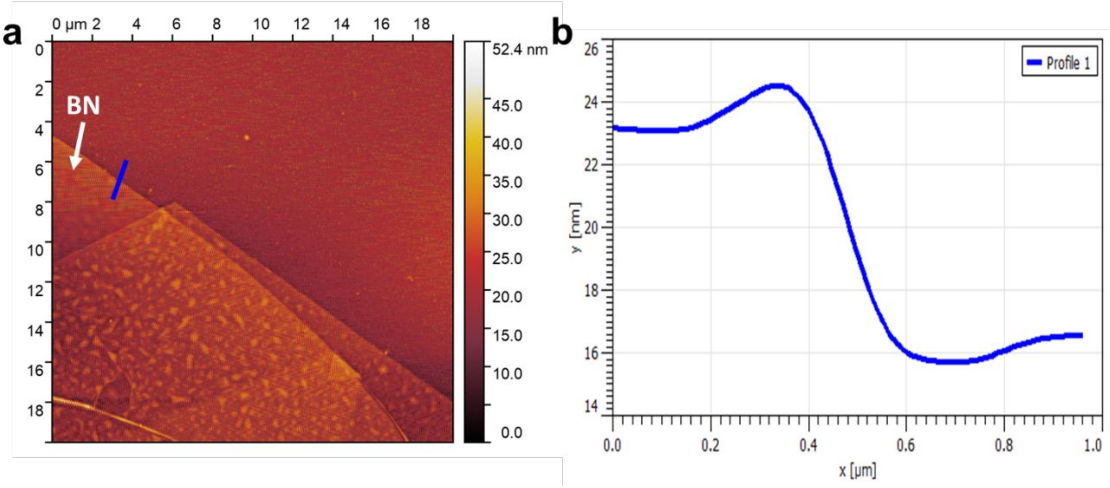

Figure S10. (a) Atomic force microscope (AFM) topography measurement of a BN flake used as the top dielectric for our device fabrication. (b) The step height profile of the BN flake edge (blue line in (a)) can be used to determine the BN thickness.

As shown in Fig. R1, the thickness of the hBN flake is around 6.2 nm (about 10 layers). We thus estimate the carrier density based on a parallel plate capacitance model: $C = \frac{\varepsilon_r \varepsilon_0 A}{d}$, in which the thickness of hBN $d = 6.2nm$, and the dielectric constant of hBN $\varepsilon_r = 3.78$ are used[10]. The capacitance is calculated to be $0.54\ \mu F/cm^2$. As a result, the additional voltage shift of 1 V from the charge neutral point will introduce a carrier density of $3.4 \times 10^{12} cm^{-2}$.

Section S12. DFT calculation

Two different models were constructed for the alloy. The first was the C_{3v} Janus structure with 50% S. The second alloy was modeled with a 2x2 supercell of the TMD structure. One and two pairs of Se atoms were replaced with S atoms to create alloys with 25% S and 50% S, respectively. Here, pair refers to chalcogen atoms with the same in-plane position but on opposite sides of the W atom in the out of plane direction. The Raman calculations were performed using Quantum Espresso[11] and Castep[12] under the local density approximation (LDA) with norm conserving pseudopotentials and a plane wave basis up to an energy cutoff 1224 eV. The lattice constants and atomic positions were fully relaxed with a force convergence threshold of 0.00025 eV/ Å. The Brillouin zone was sampled with a 12 x 12 gamma centered k-point grid. Density functional perturbation theory (DFPT) with linear response was used to calculate the vibrational modes at the gamma point. The Raman coefficients were obtained from the second order response with respect to an electric field[13]. In the Janus structure, four Raman active modes were found: one in-plane E mode at 205.4 cm^{-1}, one out of plane A_1 mode at 282 cm^{-1}, one in plane E at 334.7 cm^{-1}, and one A_1 out of plane at 421.3 cm^{-1}. None of these modes are close to the frequencies we have found in the monolayer $WS_{0.6}Se_{1.4,}$ suggesting the synthesized structure is closer to the second alloy.

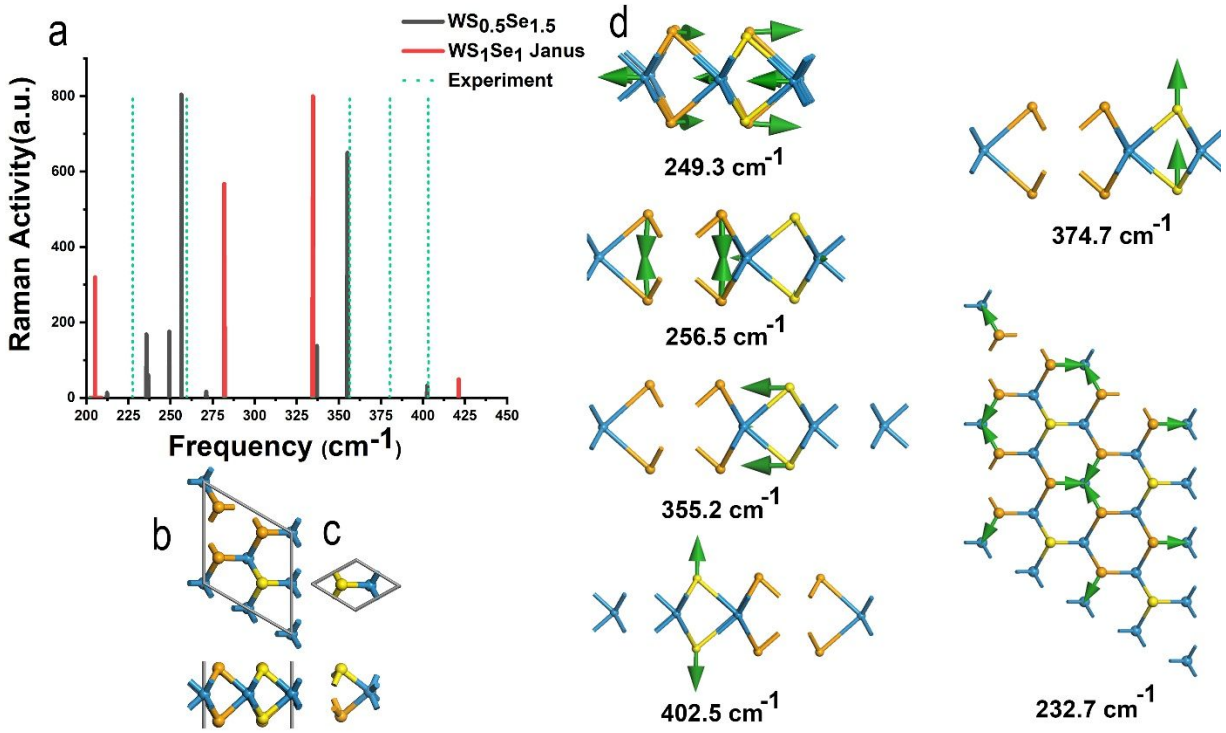

Figure S11 (a) Raman activity of first principles calculations of $WS_{0.5}$ $Se_{1.5}$ and Janus WS_1Se_1 compared with the experiment $WS_{0.6}Se_{1.4}$. (b) Top and side views of simulated $WS_{0.5}Se_{1.5}$ and (c) Janus WS_1Se_1. W atoms: blue. S atoms: yellow. Se atoms: orange. (d) Simulated vibrations modes of $WS_{0.5}$ $Se_{1.5}$ close to those obtained experimentally.

Band structure calculations were carried out in Quantum Espresso[11] with the PBE[14] functional because it generally gives better values for the spin-orbit splitting in TMDs than LDA. The lattice constants and atomic positions were fully relaxed with the PBE functional with a force convergence threshold of 0.00025 eV/Å. Norm conserving pseudopotentials constructed with the Optimized Norm-Conserving Vanderbilt (ONCV) method[15] were used. The wavefunctions were expanded in a plane wave basis up to a cutoff energy of 1088 eV and the Brillouin zone was sampled with a 7x7 Monkhorst-Pack[16] k-point mesh.

Reference

1. Pizzocchero, F., Gammelgaard, L., Jessen, B. S., Caridad, J. M., Wang, L., Hone, J., Bøggild, P. & Booth, T. J. 2016 The hot pick-up technique for batch assembly of van der Waals heterostructures. *Nat. Commun.* **7,** 1689–1699
2. Castellanos-Gomez, A., Buscema, M., Molenaar, R., Singh, V., Janssen, L., van der Zant, H. S. J. & Steele, G. A. 2014 Deterministic transfer of two-dimensional materials by all-dry viscoelastic stamping. *2D Mater.* **1,** 011002
3. Plechinger, G. *et al.* 2016 Trion fine structure and coupled spin-valley dynamics in monolayer tungsten disulfide. *Nat. Commun.* **7,** 12715
4. Plechinger, G. *et al.* 2016 Excitonic Valley Effects in Monolayer WS2 under High Magnetic Fields. *Nano Lett.* **16,** 7899–7904
5. Nagler, P. *et al.* 2018 Zeeman Splitting and Inverted Polarization of Biexciton Emission in Monolayer WS2. *Phys. Rev. Lett.* **121,** 57402
6. Erben, D., Steinhoff, A., Schönhoff, G., Wehling, T., Gies, C. & Jahnke, F. 2018 *Excitation-induced transition to indirect band gaps in atomically thin transition metal dichalcogenide semiconductors*. (arXiv:1804.08427v1, 2018).
7. Scharf, B., Dinh Van, T., Žutić, I. & Dery, H. 2018 *Dynamical Screening of Excitons in Monolayer Transition-Metal Dichalcogenides*. (arXiv:1801.06217v1, 2018).
8. Tuan, D. Van, Scharf, B., Igor, Ž. & Dery, H. 2017 Marrying Excitons and Plasmons in Monolayer Transition-Metal Dichalcogenides. *Phys. Rev. X* **041040,** 1–19
9. Wang, G., Chernikov, A., Glazov, M. M., Heinz, T. F., Marie, X., Amand, T. & Urbaszek, B. 2018 Colloquium: Excitons in atomically thin transition metal dichalcogenides. *Rev. Mod. Phys.* **90,** 21001
10. Laturia, A., Van de Put, M. L. & Vandenberghe, W. G. 2018 Dielectric properties of hexagonal boron nitride and transition metal dichalcogenides: from monolayer to bulk. *npj 2D Mater. Appl.* **2,** 6
11. Wentzcovitch, P. G. *et al.* 2009 QUANTUM ESPRESSO: a modular and open-source software project for quantum simulations of materials. *J. Phys. Condens. Matter* **21,** 395502
12. 2005 First principles methods using CASTEP . *Zeitschrift für Kristallographie - Crystalline Materials* **220,** 567
13. Lazzeri, M. & Mauri, F. 2003 First-Principles Calculation of Vibrational Raman Spectra in Large Systems: Signature of Small Rings in Crystalline Si02. *Phys. Rev. Lett.* **90,** 36401
14. Perdew, J. P., Burke, K. & Ernzerhof, M. 1996 Generalized gradient approximation made simple. *Phys. Rev. Lett.* **77,** 3865–3868
15. Schlipf, M. & Gygi, F. 2015 Optimization algorithm for the generation of ONCV pseudopotentials. *Comput. Phys. Commun.* **196,** 36–44
16. Monkhorst, H. J. & Pack, J. D. 1976 Special points for Brillouin-zone integrations. *Phys. Rev. B* **13,** 5188–5192